

Ultrahigh-sensitivity Graphene-based Strain Gauge Sensor: Fabrication on Si/SiO₂ and First-principles Simulation

Mohammed Gamil,^{1,2} Ahmed M. R. Fath El-Bab,^{3,4}
Ahmed Abd El-Moneim,¹ and Koichi Nakamura^{1,5,*}

¹Department of Materials Science and Engineering, Egypt-Japan University of Science and Technology,
New Borg El-Arab, Alexandria 21934, Egypt

²Shoubra Faculty of Engineering, Benha University, Cairo 11629, Egypt

³Department of Mechatronics and Robotics, Egypt-Japan University of Science and Technology,
New Borg El-Arab, Alexandria 21934, Egypt

⁴Department of Mechanical Engineering, Faculty of Engineering, Assiut University, Assiut 71516, Egypt

⁵Center for the Promotion of Interdisciplinary Education and Research, Kyoto University,
Kyoto 615-8540, Japan

(Received April 4, 2018; accepted July 23, 2018)

Keywords: graphene, chemical vapor deposition, strain gauge, gauge factor, piezoresistive sensors, MEMS devices, first-principles calculation

Monolayer and multilayer graphene films have been grown on a Cu substrate by chemical vapor deposition (CVD) and then transferred onto a SiO₂/Si substrate using polymethyl methacrylate (PMMA) to fabricate an ultrasensitive graphene-based strain gauge sensor. The graphene films were patterned using a CO₂ laser beam. The sensitivity and temperature dependence of the gauge factor (GF) of the fabricated sensors were examined at different applied strains and operating temperatures up to 0.05% and 75 °C, respectively. The fabricated gauges based on monolayer and multilayer graphene films show stable GFs of 255 and 104 within the applied temperature range, respectively. The patterning technique provides an interesting, low-cost, fast, and high-throughput process to realize scalable microfabrication for highly sensitive strain sensors with good temperature stability based on graphene piezoresistivity. A theoretical simulation of the GF of monolayer graphene has also been carried out on the basis of first-principles calculation. Simulation results follow the measured GFs in our experiment and other references.

1. Introduction

Strain measurement via strain gauges is an important analysis probe in various engineering applications. The sensitivity of the measurement is determined by the gauge factor (GF), which results from dividing the relative resistance change of a conductive material by the applied strain.^(1,2) The piezoresistance-based strain gauge made of silicon is considered the most successful micro-electromechanical system (MEMS) device for measuring strain. Silicon is a piezoresistive material with a high GF.⁽¹⁾ However, the GF of silicon is not stable

*Corresponding author: e-mail: koichi@cpier.kyoto-u.ac.jp

<https://doi.org/10.18494/SAM.2018.1955>

with temperature change. Recently, graphene has been presented as a potential piezoresistive material that can withstand a large strain and is stable up to a temperature of 700 °C, aside from having a very high carrier mobility.^(3–18) Moreover, graphene is compatible with the wafer level owing to its two-dimensional architecture, suggesting that the material could be a promising template for novel microfabrication processes.

Chemical vapor deposition (CVD) is a simple, scalable, and cost-efficient method of preparing single- and few-layer graphene films on various substrates; it opens a new route to the large-area production of high-quality graphene films for practical applications. In this regard, a large-area growth of graphene films via CVD on copper (Cu) foils has been successful, and subsequently, a polymethyl methacrylate (PMMA) polymer has been used to aid the transfer of the developed graphene film to a silicon dioxide/silicon (SiO₂/Si) substrate.^(3–5) This process yields also a graphene film with low densities of cracks and tears and excellent electrical conductivity, which is suitable for the microfabrication of a new generation of graphene-based devices.

Recently, we have reported the first production of a defective laser-reduced graphene oxide film with a multilayer structure for the microfabrication of a strain gauge sensor using a carbon dioxide (CO₂) laser beam to simultaneously reduce and pattern a drop-casted and pre-dried graphene oxide film dispersed over a flexible polyethylene terephthalate (PET) substrate.^(6–8) A commercially available laser printing machine was adopted, enabling reliable, high-throughput production without special preparation or adjustment while using large patterning areas and a thick film. This further lowers the production cost.

Thus far, many researchers have developed graphene-based strain gauges and reported their GFs. Zheng *et al.* stated that the GF of mechanically exfoliated graphene on a Si/SiO₂ substrate ranges from 10 to 15, depending on its number of layers,⁽⁹⁾ but their production method has a low yield and is nonreproducible and time-consuming. Lee *et al.* reported that the GF of graphene grown by CVD over a copper film deposited on a Si/SiO₂ substrate is 6.1.⁽¹⁰⁾ Chen *et al.* reported that the GF of the mechanically exfoliated monolayer graphene over a silicon chip is 150.⁽¹¹⁾ Fu *et al.* measured a GF of 151 for monolayer graphene prepared by CVD, then transferred graphene to polydimethylsiloxane (PDMS) as a flexible substrate.⁽¹²⁾ Zhao *et al.* indicated that they achieved a tunable GF of up to 300 for multilayer graphene-based strain sensors.⁽¹³⁾ As a maximum value, Hosseinzadegan *et al.* reported that the GF of monolayer graphene is 18000,⁽¹⁴⁾ but it seems to be out of standard owing to some reasons. These reports provide a clear indication of the importance of utilizing graphene in the microfabrication of strain gauge sensors. However, these methods are not reproducible and cannot be used for commercial applications.

In this work, a highly sensitive strain gauge based on graphene piezoresistivity, by producing graphene with a large area via a reproducible fabrication method, such as CVD in order to obtain a low-cost, commercial, and high-GF strain sensor, is presented. A new patterning method for graphene was proposed to achieve the target of low cost. In addition to the experimental work, we simulated the strain GF for the ideal graphene sheet model on the basis of first-principles electronic band calculation. The strain orientation dependence on GF and the linearity of resistivity against the strain shall be discussed in this paper.

2. Experimental Methods

2.1 Graphene preparation and characterization

The as-received graphene films of monolayer and multilayer structures were initially grown by CVD on a 25- μm -thick polycrystalline Cu foil in a silica tube furnace. The tube was heated to 1000 °C in the presence of 2 sccm hydrogen flow while keeping the pressure at 40 mTorr and holding the temperature for 10 min before introducing 10–35 sccm of methane (CH_4) for 30 min at 500 mTorr. Low-concentration or diluted CH_4 was used for the development of a few-layer graphene film. After the furnace was self-cooled to room temperature, PMMA was used to aid the transfer of graphene to the Si/SiO₂ surface. Details of the fabrication and transfer processes of graphene films have been reported in our previous study.⁽¹⁵⁾

To insure the quality and number of graphene layers, the deposited films were characterized by optical microscopy (Keyence, VHX-1000), SEM (JEOL, JSM-6010LV), AFM (Bruker AFM), and Raman spectroscopy (Lambda Solutions, Dimension-P1).

2.2 Strain gauge fabrication and GF measurement

To evaluate the performance of the films under the applied strain effect, the graphene-based piezoresistive strain gauge sensor was fabricated in three consecutive steps given in Fig. 1(a): I. graphene patterning, where the films were patterned into strips of about 300 μm width, as

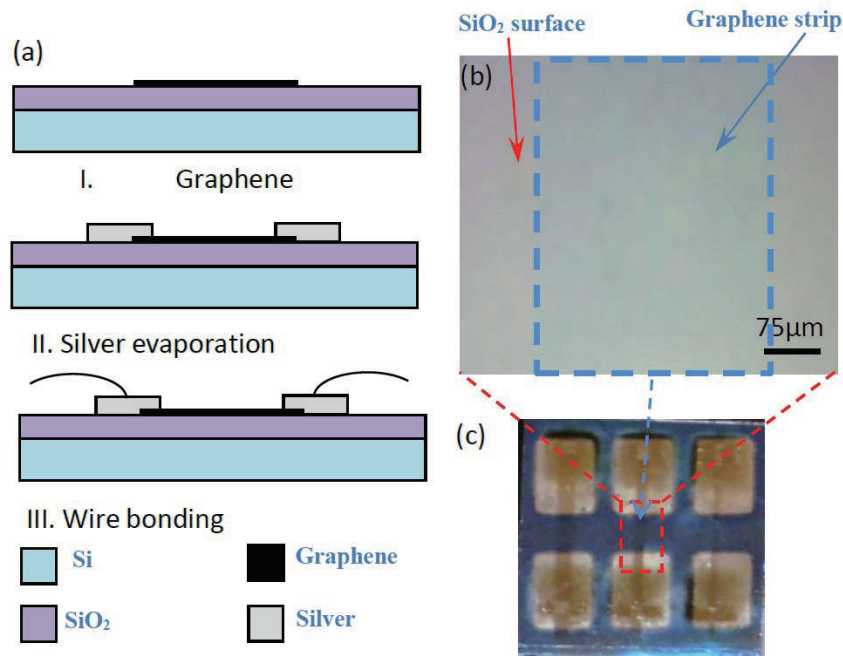


Fig. 1. (Color online) (a) Fabrication processes of a graphene-based piezoresistive strain gauge. (b) Graphene patterned by a laser machine. (c) Evaporation of silver electrodes.

shown in Fig. 1(b), using a laser printing machine (Universal Laser Systems, VLS3.50) with an optical system focal length of 51 mm at a pulse density of 393.7 p/cm (1000 PPI); II. creation of silver pads to form a good medium for electrical connection, where a 2- μm -thick silver film with a length of 3 mm was deposited by thermal evaporation, as shown in Fig. 1(c); III. silver paste wire bonding to create output connection terminals to apply direct current (DC) and measure the output voltage simultaneously.

A schematic diagram of the test rig designed to measure the free-strain graphene resistance (R_g) and the change in graphene resistance (ΔR_g) at an applied strain (ε) is given in Fig. 2. The test rig consists of a cantilever beam fixed from one end and free from the other end, as shown in Fig. 2(a). The strain ε is applied by the act of applying force on the free end of the cantilever beam. For determining the resistance R_g and ΔR_g , DC was applied to the terminals of the graphene using a Keithley Model 6221 DC current source. The output voltage was measured using a Keithley Model 2182A nanovoltmeter (four-point probe), as shown in Fig. 2(b).

The actual strain of the deformed cantilever and the corresponding ΔR_g were measured using commercial strain gauges with a full Wheatstone bridge for maximum sensitivity and temperature compensation. Commercial strain gauges were placed in a position with the same uniaxial strain applied to the graphene strain sensor, as shown in Fig. 2(a).

An epoxy bond (Araldite Rapid) was used to bond the SiO_2/Si wafer (graphene-based strain gauge) on the surface of the steel cantilever beam. In order to apply the glue, all surfaces to be glued were made clean, dry, and dust-free. Then, equal amounts of the two components of the epoxy bond were dispensed onto a clean mixing surface, mixed for 5 min with the spatula provided, and applied to the surface of the steel cantilever beam. Then, the SiO_2/Si substrate was firmly pressed and left for at least 20 min. To glue the commercial strain gauges, all surfaces must be clean, dry, and dust-free. Then, a small amount of glue was dispensed onto the steel cantilever beam surface. After that, we pressed it on the commercial gauges firmly and kept pressing for nearly 2 min until it dried using the nonsticking paper attached to the commercial strain gauges.

To test the graphene-based strain gauge sensors at different temperatures, the test rig was inserted inside a furnace with a digital temperature controller in order to adjust the tested temperature.

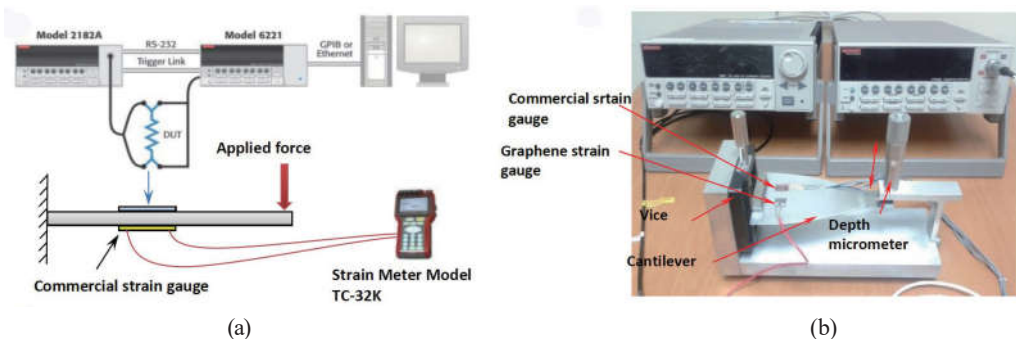


Fig. 2. (Color online) (a) Schematic diagram of the circuit components used in the strain measurement and (b) detailed structure of the test rig for graphene strain gauge measurement.

3. Computational Method

3.1 First-principles calculation

Under the periodic boundary condition, the unit cell of the ideal two-dimensional monolayer graphene model consists of two carbon atoms. Under the strain-free condition, the C–C bond length is equal to $a/3^{1/2}$, where a is a lattice constant. When a uniaxial tensile strain ε with an angle θ ($0^\circ < \theta < 30^\circ$) is added to the ideal graphene model, as shown in Fig. 3, the translational vectors \mathbf{a}_1 and \mathbf{a}_2 of the unit cell can be represented with the Poisson's ratio $v(\theta)$ by

$$(\mathbf{a}_1 \ \mathbf{a}_2) = \mathbf{R}(\theta) \begin{pmatrix} 1-v(\theta)\varepsilon & 0 \\ 0 & 1+\varepsilon \end{pmatrix} \mathbf{R}(\theta)^{-1} \begin{pmatrix} a/2 & -a/2 \\ \sqrt{3}a/2 & \sqrt{3}a/2 \end{pmatrix}, \quad (1)$$

where $\mathbf{R}(\theta)$ is a two-dimensional rotation matrix,

$$\mathbf{R}(\theta) = \begin{pmatrix} \cos\theta & -\sin\theta \\ \sin\theta & \cos\theta \end{pmatrix}. \quad (2)$$

The tensile-strained structure for each θ was obtained by the relaxation of atomic forces on carbon atoms and the optimization of $v(\theta)$ by first-principles calculation with the fixed ε .

The first-principles electronic band structures of the two-dimensional graphene models were calculated using the VASP program package^(19,20) based on the density functional theory (DFT).⁽²¹⁾ For the DFT exchange-correlation interaction, the generalized-gradient approximation method was used with the Perdew–Wang (PW91) functional.^(22,23) By introducing a vacuum space of 10

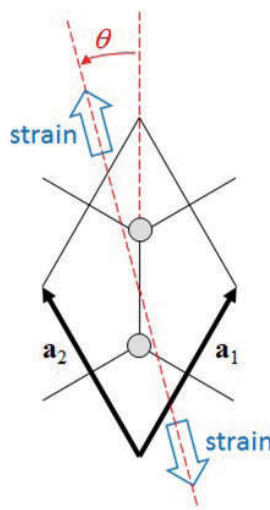


Fig. 3. (Color online) Uniaxial tensile strain on unit cell of graphene sheet for θ direction ($0^\circ \leq \theta \leq 30^\circ$).

Å vertical to the graphene sheet, the three-dimensional supercell approximation technique was adopted with ultrasoft pseudopotentials.⁽²⁴⁾ The cutoff energy for wave functions of electrons with plane-wave expansion was set at 30 Ry (408 eV). For geometrical optimization, the k-point sampling was set by the Monkhorst–Pack $6 \times 6 \times 1$ grids.⁽²⁵⁾

3.2 Simulation of GF

The strain-free monolayer graphene sheet has a Dirac cone around the k-point, the corner of the first Brillouin zone.⁽²⁶⁾ Carrier electrons and holes are localized on the Dirac cone, and the electrical conductivity tensor \mathbf{G} or the electrical resistivity tensor ρ can be represented in terms of carrier concentrations and their effective masses by

$$\mathbf{G} = (\rho)^{-1} = e^2 \left[n(\mathbf{m}_e^*)^{-1} \tau_e + p(\mathbf{m}_h^*)^{-1} \tau_h \right], \quad (3)$$

where n is the carrier electron concentration, p is the hole concentration, \mathbf{m}_e^* and \mathbf{m}_h^* are the effective mass tensors, τ_e and τ_h are the relaxation time tensors, and e^2 is the square of the absolute value of the elementary electric charge.⁽²⁷⁾ The subscripts e and h respectively denote electron and hole carriers. The concentrations n and p are followed by the Fermi–Dirac distribution with the Fermi energy E_F and the temperature T as follows:

$$n = \frac{2}{V} \sum_{\mathbf{k}} w_{\mathbf{k}} \left[\exp\left(\frac{E_{n,\mathbf{k}} - E_F}{k_B T}\right) + 1 \right]^{-1}, \quad (4)$$

$$p = \frac{2}{V} \sum_{\mathbf{k}} w_{\mathbf{k}} \left[\exp\left(\frac{E_{p,\mathbf{k}} - E_F}{k_B T}\right) + 1 \right]^{-1}, \quad (5)$$

and \mathbf{m}_e^* and \mathbf{m}_h^* are given by

$$(\mathbf{m}_{e,h}^*)^{-1} = \pm \frac{1}{\hbar^2} \begin{pmatrix} \partial^2 E_j / \partial k_l^2 & \partial^2 E_j / \partial k_l \partial k_t \\ \partial^2 E_j / \partial k_t \partial k_l & \partial^2 E_j / \partial k_t^2 \end{pmatrix}_{\mathbf{k}=K}, \quad (6)$$

where $E_{n,\mathbf{k}}$ and $E_{p,\mathbf{k}}$ are the conduction band and valence band energies of the Dirac cone at the \mathbf{k} point, k_l and k_t are the longitudinal and transverse coordinates of the reciprocal lattice space for the tensile strain, respectively, V is the graphene volume per unit cell, and \hbar is equal to Planck's constant divided by 2π . On the right-hand side in Eq. (6), a positive sign is adopted for carrier electrons ($j = n$) and a negative sign for holes ($j = p$). For the relaxation times, we have adopted the approximation that all band relaxation times are equal and constant regardless of strain,^(28,29) because the variation rate of carrier conductivity can be easily and adequately

represented in consideration of the cancellation of most of the band relaxation times.

The longitudinal GF is given by

$$GF = \frac{\Delta R_g}{R_g \epsilon} = \frac{\Delta \rho_l}{\rho_l^0 \epsilon}, \quad (7)$$

where ρ_l^0 is the longitudinal resistivity without strain and $\Delta \rho_l$ is the variation in ρ_l^0 due to the strain ϵ .

4. Results and Discussion

4.1 Film characterization

To characterize the structure, growth uniformity, and transfer efficiency of the developed and transferred films, the films were characterized using Raman, SEM, and AFM characterization techniques.

Figures 4(a) and 4(b) show the Raman spectra of the synthesized graphene films on the SiO₂/Si substrate. In principle, three predominant peaks could be observed in the spectra presented in Fig. 4: the 2D band at 2720 cm⁻¹, the G band at 1590 cm⁻¹, and the D band at 1350 cm⁻¹. The G and 2D bands are assigned as bands typical of the graphene layers.^(30–33) In general, the presence of the D band is generally associated with the number of defects in the crystalline structure of the graphene layers. Furthermore, a higher $I(2D)/I(G)$ peak ratio as well as an increased intensity and a decreased full width at half maximum (FWHM) of the 2D band are commonly employed to indicate the restoration of sp^2 -hybridized C–C bonds in graphitic structures and the presence of a fewer number of graphene layers.^(30,34) In Fig. 4(a), the Raman spectrum exhibits an $I(2D)/I(G)$ peak ratio far larger than unity and a single Lorentzian fit of the 2D band typical of the scarce formation of multilayer graphene and characteristic of the monolayer. It is also worth noting that the intensity of the D band (1350 cm⁻¹) is below the Raman detection level, which confirms that the synthesized film is largely free of structural

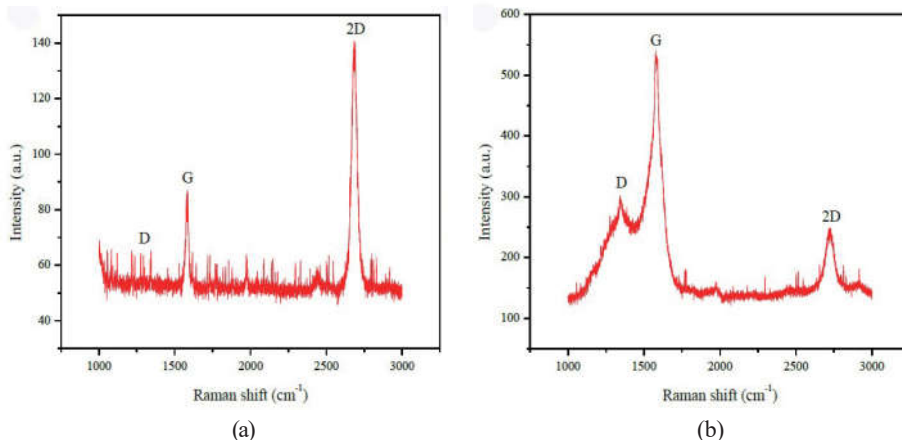


Fig. 4. (Color online) Raman spectra of (a) monolayer and (b) multilayer graphene films.

defects. The Raman spectrum in Fig. 4(b) exhibits an $I(2D)/I(G)$ peak ratio far smaller than unity with a clear detection of the D band, reflecting the formation of defective multilayers of graphene.

The growth uniformity and transfer efficiency of the developed and transferred films were further evaluated by SEM and AFM. Figure 5 shows SEM images of monolayer and multilayer graphene films on a SiO_2/Si substrate. As seen in Fig. 5(a), a uniform light grey color contrast of the polycrystalline monolayer graphene image covers about 95% of the graphene film, where the rest of the area and dark spots were probably related to the bilayer and trilayer graphenes on existing defects on monolayer graphene. The image also clearly reveals the excellent continuity with the absence of wrinkles over a millimeter length scale. This indicates that the film has excellent thickness uniformity on the SiO_2/Si substrate. The domain size for the monolayer graphene is typically around 10 μm , which is likely due to the grain size of the polycrystalline Cu catalyst used in the synthesis process. On the other hand, Fig. 5(b) shows a nonuniform growth of the transferred multilayer graphene film on the SiO_2/Si substrate.

Figure 6 shows AFM images of monolayer and multilayer graphene films deposited on the Si/SiO_2 surface without filtering or smoothing for a 600 nm^2 sweeping area. Peaks with heights of a few nanometers are observed for monolayer and multilayer graphene films across all the graphene samples, indicating that the graphene monolayer and multilayer largely follow the underlying substrate morphology, which is a good indication of the good adhesion force between the prepared graphene and the SiO_2 surface and also gives a clue to the successive transfer process by the PMMA-assisted transfer method.⁽³⁵⁾

4.2 GF measurement

To determine the GF of the graphene, different forces were applied to the free end of the cantilever beam carrying monolayer and multilayer graphene films using a depth micrometer, as shown in Fig. 7. The strain was measured using a commercial strain gauge that was placed in the same stress area of the graphene. As seen, the strain change is from 0 to 0.05% and the corresponding electrical resistance change is from 269 to 301 Ω for the monolayer graphene

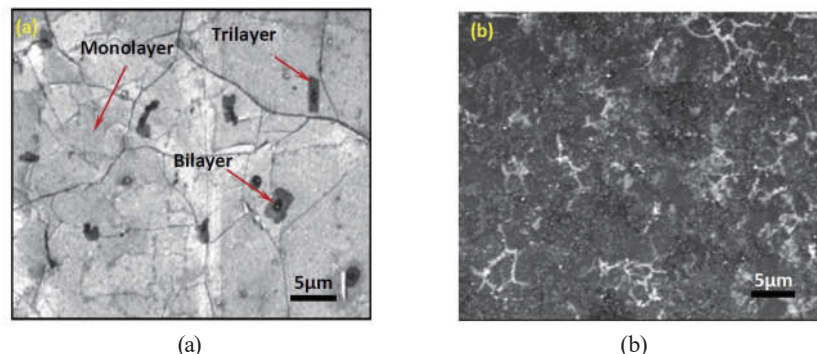


Fig. 5. (Color online) SEM images of (a) monolayer and (b) multilayer graphene films transferred onto SiO_2/Si substrate.

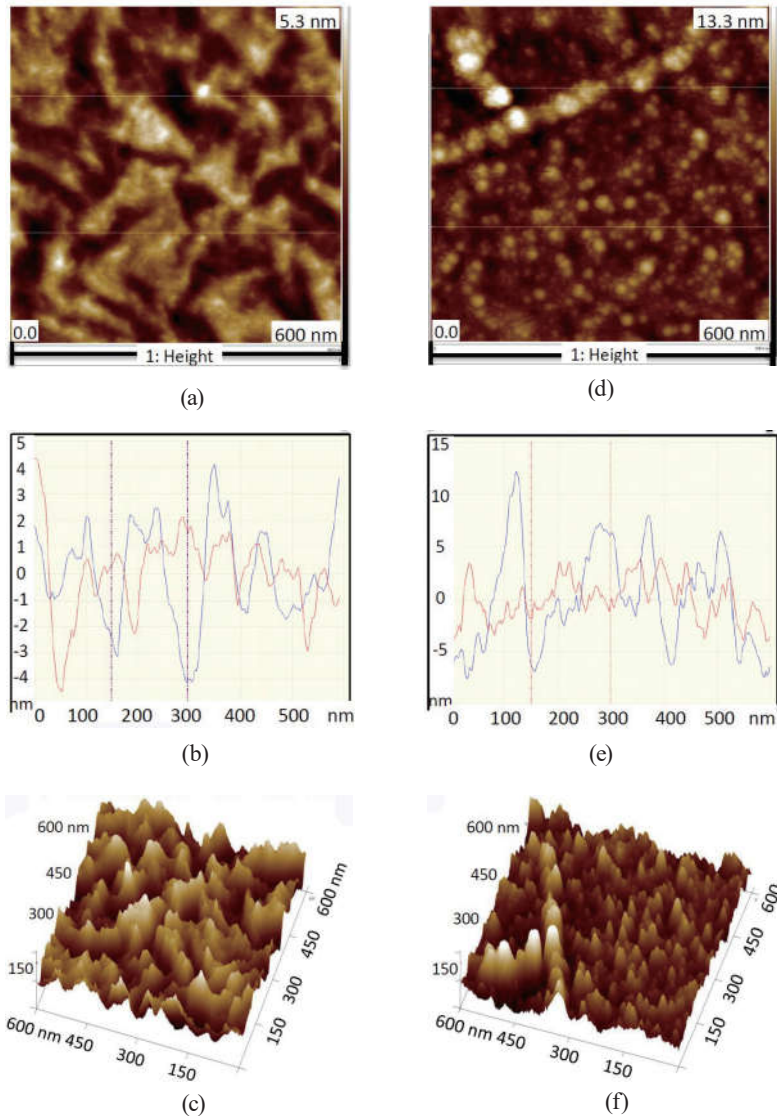


Fig. 6. (Color online) AFM images of graphene on SiO_2 : (a) monolayer 2D image, (b) surface profile for monolayer, (c) monolayer 3D image, (d) multilayer 2D image, (e) surface profile for multilayer, and (f) multilayer 3D image.

film and from 670 to 705 Ω for the multilayer graphene film. The change in electrical resistance was clear and reproducible after multiple repetitions and disregarding the odd results, which shows that the devices are rigid enough to sustain strain. Each point on the graph represents the average of three readings.

The longitudinal GF was calculated from Eq. (7). Interestingly, the estimated GF of the monolayer graphene strain gauge at 25 °C is about 255, which is higher than the reviewed values for monolayer graphene,^(9–12,36) and opens a new era for piezoresistive strain gauges with very high sensitivity, while the measured GF of the multilayer graphene strain gauge at the same temperature is about 104. Fortunately, the GFs of the monolayer and multilayer graphene films are stable under different strains, as shown in Fig. 8.

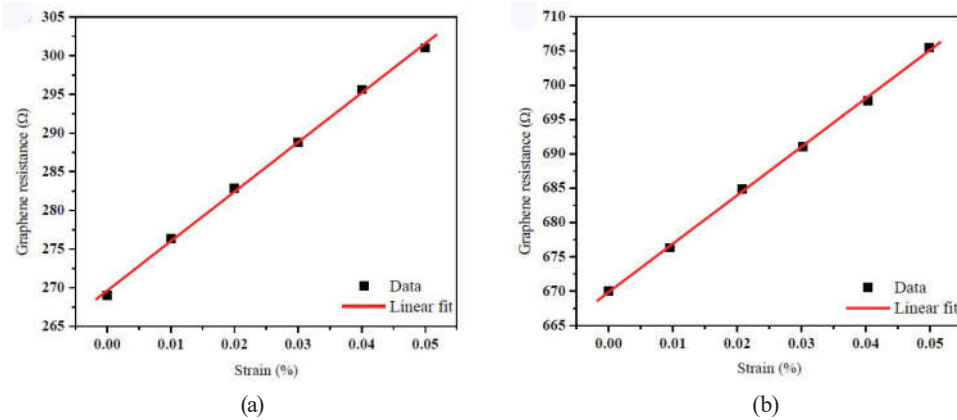


Fig. 7. (Color online) Electrical resistance measurements of (a) monolayer and (b) multilayer graphene films under different applied strains.

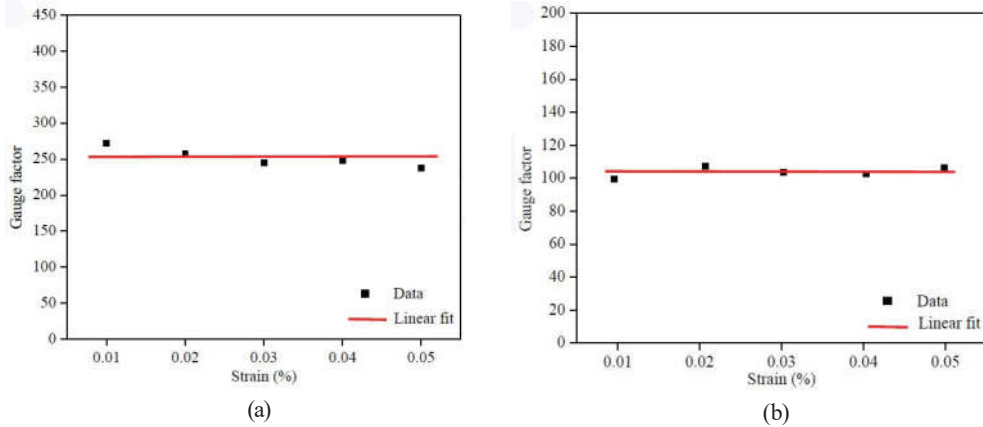


Fig. 8. (Color online) Relationship between applied strain and GF for (a) monolayer and (b) multilayer graphene films.

Figure 9 presents the effect of temperature increase on the resistance change for the monolayer and multilayer graphene films. It is clear that the graphene resistances for the monolayer and multilayer decrease slightly with increasing temperature because graphene behaves similarly to a semiconductor. The heat excites free electrons and causes the electrons to move; hence, the conductivity increases.⁽¹²⁾ The GFs at 50 and 75 °C were respectively measured as 230 and 220 for the monolayer and as 99.7 and 97.7 for the multilayer. The temperature coefficients of GFs for the monolayer and multilayer can be evaluated as -0.70 and -0.13 K^{-1} , respectively, under the linear approximation. Namely, the piezoresistivity of monolayer graphene is much more sensitive to temperature than that of multilayer graphene.

4.3 Strain response of band structure

The Dirac cone in the ideal monolayer graphene collapses, and a small band gap should be observed if its symmetry is broken by strain. Table 1 shows the Poisson's ratio $v(\theta)$ and band

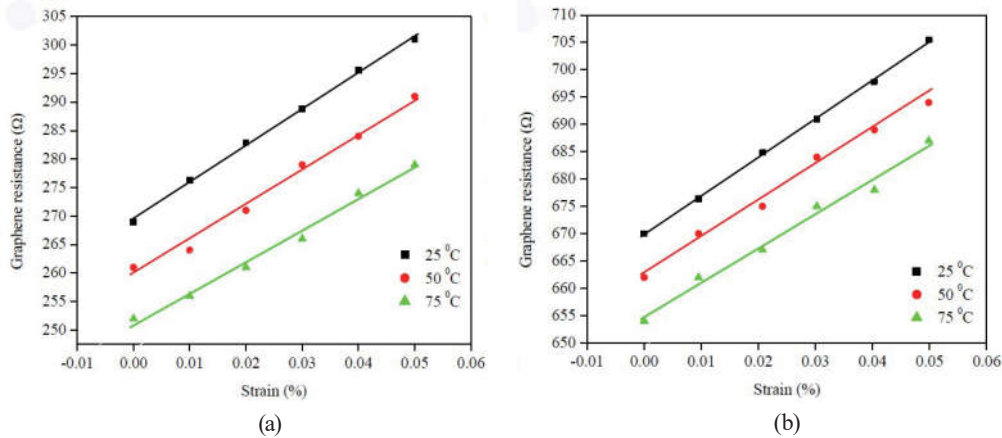


Fig. 9. (Color online) Temperature effect on resistance change of (a) monolayer and (b) multilayer graphene films.

Table 1
Poisson's ratio $\nu(\theta)$ and band gap of 1% tensile-strained graphene sheets.

θ (deg)	$\nu(\theta)$	Band gap (eV)
0	0.27	0.0387
5	0.27	0.0380
10	0.27	0.0273
15	0.26	0.0307
20	0.25	0.0268
25	0.23	0.0274
30	0.19	0.0234

gap values under the uniaxial tensile strain $\varepsilon = 0.01$ for the direction θ . The hexagonal Brillouin zone is distorted according to strain on the unit cell, while the K points, six corners of the hexagonal Brillouin zone, remain equivalent even if any strain is added. Therefore, the carrier redistributions among valleys in the conduction band and peaks in the valence band cannot occur. For the change in carrier distribution, only the decrease in carrier concentration should be observed on the basis of the band gap generated by the strain. Figure 10 shows the strain dependence on the band gap for $\theta = 0$, and the high linearity of the band gap against the strain has been observed.

The band dispersion for a small uniaxial strain ε shows linearity similarly to the Dirac cone except for the vicinity of the K points, while it is possible to do second-order derivatives in the vicinity of the K points. This image can be related to the asymptotes and vertices of a hyperbola. For the conduction band, as shown in Fig. 11(a), when the slopes of asymptotes are $+u$ and $-v$ ($u, v > 0$) for the $+k$ and $-k$ directions, respectively, the hyperbola curves of the conduction band with the band gap E_g can be represented as

$$E^2 - (u - v)Ek - uvk^2 = E_g^2 / 4 \quad (E > 0), \quad (8)$$

where the K point and its band energy are defined as $k = E = 0$. The band energies in the

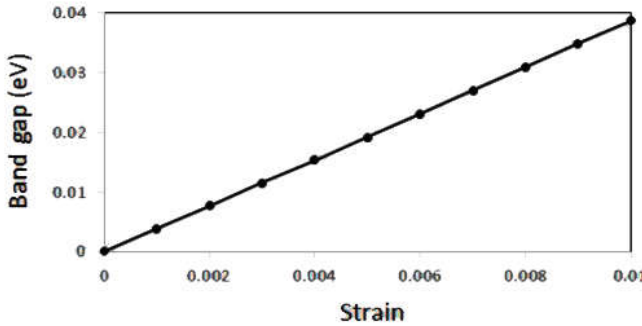


Fig. 10. Band gap of tensile-strained graphene sheet with respect to strain at $\theta = 0^\circ$.

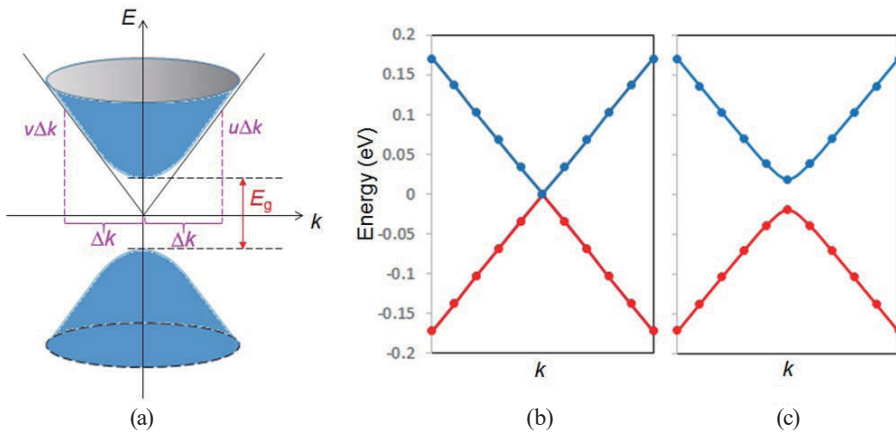


Fig. 11. (Color online) (a) Image of band dispersion of strained graphene sheet and band energies of (b) strain-free and (c) strained ($\theta = 0^\circ$) graphene sheets in the vicinity of K point. Plots in (b) and (c) are actual calculation values, and curves are fitted using Eq. (8).

vicinity of the K point are completely given by Eq. (8), as shown in Figs. 11(b) and 11(c). The second derivative of Eq. (8) at the K point is given as

$$\left(\frac{d^2E}{dk^2} \right)_{k=0} = 2uv/E_g, \quad (9)$$

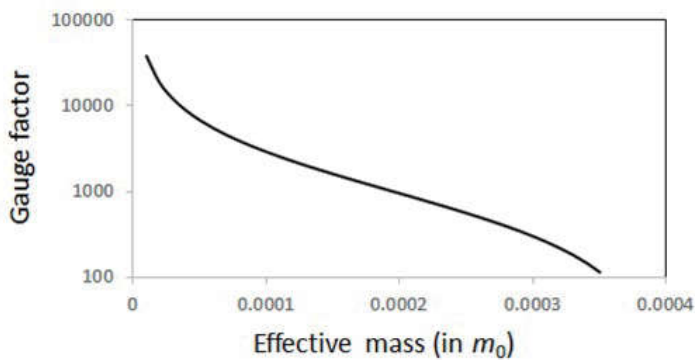
by using the conditions $dE/dk \approx 0$ and $E = E_g/2$ at $k = 0$. Namely, the effective mass m_e^* in Eq. (6) should be proportional to the band gap E_g if the slopes of asymptotes are constants. According to Fig. 10, the strain response of the effective mass is linear. The same consideration can be applied for the valence band.

Table 2 shows the effective masses for 1% tensile-strained monolayer graphene for each strain direction. The effective mass for $\varepsilon = 0.01$ has an order of $10^{-3} m_0$, where m_0 is the electron rest mass, and the following results have been confirmed: (i) the longitudinal and transverse effective masses for strain direction are almost equal to each other; (ii) the effective masses of carrier electrons and holes are almost equal to each other; (iii) the strain direction dependence of the effective mass is relatively small.

Table 2

Effective masses of carrier electron and hole in unit of m_0 for 1% tensile-strained graphene sheets.

θ (deg)	Carrier electron		Hole	
	Longitudinal	Transverse	Longitudinal	Transverse
0	0.00508	0.00500	0.00503	0.00495
5	0.00500	0.00490	0.00495	0.00485
10	0.00362	0.00351	0.00358	0.00347
15	0.00410	0.00394	0.00405	0.00389
20	0.00358	0.00344	0.00356	0.00340
25	0.00368	0.00352	0.00364	0.00347
30	0.00311	0.00301	0.00306	0.00298

Fig. 12. Calculated longitudinal GF of ideal graphene sheet model due to strain $\varepsilon = 0.001$, as a function of effective mass of external strain-free graphene, m_{sf}^* . The data are averaged for all angles ($0^\circ \leq \theta < 360^\circ$).

4.4 Qualitative and quantitative characteristics of GF

The calculated longitudinal GFs of the ideal graphene monolayer sheet model are shown in Fig. 12, as a function of effective mass for the external strain-free graphene, m_{sf}^* . Generally, even the external strain-free graphene sheet does not have an exactly planar structure. It is a wavy sheet with breaking of an exact symmetry by internal strain, called a ripple structure.⁽³⁷⁾ Lattice defects and vibrations also break the exact symmetry, so the m_{sf}^* of carrier electrons and holes should not be exactly zero. The numerical order of effective masses for external strain-free graphene correlates with the conditions of the graphene sheet such as the deposition method and substrate material. On the other hand, the effect of a ripple structure with internal strain in the external tensile-strained graphene sheet is too small to correct the effective mass.

For the graphene sheet, the resistivity is not affected so much by the change in carrier concentration caused by the increase in the band gap. Practically, the high piezoresistivity is based on the drastic increase in effective mass due to the collapse of the Dirac cone owing to the external strain. The experimental result indicating that the resistivity of the graphene sheet has linearity to the strain can be associated with the proportional relationship between the effective mass and the external strain, as discussed in the previous section. The calculated GF

is very sensitive to strain, as shown in Fig. 12, and the general measured GFs of 150–255 for monolayer graphene, in this study and in Refs. 11 and 12, are derived in the case of $m_{sf}^* \approx 3 \times 10^{-4} m_0$. This m_{sf}^* value corresponds to the band gap E_g of 0.00025 eV in terms of Eq. (9), and the small E_g can be reproduced by considering the internal strain, lattice defects and vibrations, and ripple structure. Even the GF of 18000 in Ref. 14 can also be reproduced, if the external strain-free graphene would be very close to the internal strain-free exact-symmetry structure, where $m_{sf}^* \approx 10^{-5} m_0$.

5. Conclusions

A graphene monolayer with a large area was developed for strain gauge sensor application using a CVD complement by a transfer method. The deposited graphene monolayer showed great continuity with fewer defects on the SiO₂/Si substrate with about 95% coverage. Graphene films were characterized by optical microscopy, SEM, AFM, and Raman spectroscopy. The graphene monolayer was patterned by a laser machine method, which is simple and requires no sophisticated precautions. The measured strain GFs for monolayer and multilayer graphene films were 255 and 104, respectively. These values were higher than all the reported values for graphene for strain gauge application and development by different fabrication techniques. The temperature effect on the graphene resistance and GF was examined up to 75 °C. The results showed that the resistances for single and multilayer graphene decrease with increasing temperature. On the other hand, the GF shows stable behavior with increasing temperature, which promises a new low-cost strain gauge sensor with high sensitivity and temperature stability. A theoretical simulation of the GF of monolayer graphene was also carried out on the basis of first-principles calculation. Simulation results followed the measured GFs in our experiment and other references.^(11,12,14)

Acknowledgments

This research was conducted as a Bilateral Joint Research Project funded by the Science and Technology Development Fund (STDF) in Egypt, and the Japan Society for the Promotion of Science (JSPS). The first author is deeply grateful to the Mission Sector-MOHE for providing a Ph.D. degree scholarship fund, the Materials Science and Engineering Department at E-JUST, and the Japan International Cooperation Agency (JICA) for support of this work.

References

- 1 C. S. Smith: Phys. Rev. **94** (1954) 42.
- 2 A. A. Barlian, W.-T. Park, J. R. Mallon, A. J. Rastegar, and B. L. Pruitt: Proc. IEEE **97** (2009) 513.
- 3 X. Li, W. Cai, J. An, S. Kim, J. Nah, D. Yang, R. Piner, A. Velamakanni, I. Jung, E. Tutuc, S. K. Banerjee, L. Colombo, and R. S. Ruoff: Science **324** (2009) 1312.
- 4 A. Reina, X. Jia, J. Ho, D. Nezich, H. Son, V. Bulovic, M. S. Dresselhaus, and J. Kong: Nano Lett. **9** (2009) 30.
- 5 X. Li, Y. Zhu, W. Cai, M. Borysiak, B. Han, D. Chen, R. D. Piner, L. Colombo, and R. S. Ruoff: Nano Lett. **9** (2009) 4359.

- 6 M. Gamil, H. Nageh, I. Bkrey, S. Sayed, A. M. R. Fath El-Bab, K. Nakamura, O. Tabata, and A. Abd El-Moneim: *Sens. Mater.* **26** (2014) 699.
- 7 S. Sayed, M. Gamil, A. M. R. Fath El-Bab, and A. Abd El-Moneim: *Key Eng. Mater.* **644** (2015) 115.
- 8 S. Sayed, M. Gamil, A. Fath El-Bab, K. Nakamura, T. Tsuchiya, O. Tabata, and A. Abd El-Moneim: *Sens. Rev.* **36** (2016) 140.
- 9 X. Zheng, X. Chen, J.-K. Kim, D.-W. Lee, and X. Li: *J. Micro/Nanolithogr. MEMS MOEMS* **12** (2013) 013009.
- 10 Y. Lee, S. Bae, H. Jang, S. Jang, S.-E. Zhu, S. H. Sim, Y. I. Song, B. H. Hong, and J.-H. Ahn: *Nano Lett.* **10** (2010) 490.
- 11 X. Chen, X. Zheng, J.-K. Kim, X. Li, and D.-W. Lee: *J. Vac. Sci. Technol. B* **29** (2011) 06FE01.
- 12 X.-W. Fu, Z.-M. Liao, J.-X. Zhou, Y.-B. Zhou, H.-C. Wu, R. Zhang, G. Jing, J. Xu, X. Wu, W. Guo, and D. Yu: *Appl. Phys. Lett.* **99** (2011) 213107.
- 13 J. Zhao, C. He, R. Yang, Z. Shi, M. Cheng, W. Yang, G. Xie, D. Wang, D. Shi, and G. Zhang: *Appl. Phys. Lett.* **101** (2012) 063112.
- 14 H. Hosseinzadegan, C. Todd, A. Lal, M. Pandey, M. Levendorf, and J. Park: Proc. 2012 IEEE 25th Int. Conf. Electro Mechanical Systems (IEEE, 2012) 611.
- 15 M. Gamil, O. Tabata, K. Nakamura, A. M. R. Fath El-Bab, and A. Abd El-Moneim: *Key Eng. Mater.* **605** (2014) 207.
- 16 J. Hass, R. Feng, T. Li, X. Li, Z. Zong, W. A. de Heer, P. N. First, E. H. Conrad, C. A. Jeffrey, and C. Berger: *Appl. Phys. Lett.* **89** (2006) 143106.
- 17 D. A. Areshkin, D. Gunlycke, and C. T. White: *Nano Lett.* **7** (2007) 204.
- 18 S. Watcharotone, D. A. Dikin, S. Stankovich, R. Piner, I. Jung, G. H. B. Dommett, G. Evmenenko, S.-E. Wu, S.-F. Chen, C.-P. Liu, S. T. Nguyen, and R. S. Ruoff: *Nano Lett.* **7** (2007) 1888.
- 19 G. Kresse and J. Hafner: *Phys. Rev. B* **47** (1993) R558.
- 20 G. Kresse and J. Furthmüller: *Phys. Rev. B* **54** (1996) 11169.
- 21 P. Hohenberg and W. Kohn: *Phys. Rev.* **136** (1964) B864.
- 22 J. P. Perdew and Y. Wang: *Phys. Rev. B* **45** (1992) 13244.
- 23 J. P. Perdew, J. A. Chevary, S. H. Vosko, K. A. Jackson, M. R. Pederson, D. J. Singh, and C. Fiolhais: *Phys. Rev. B* **46** (1992) 6671.
- 24 D. Vanderbilt: *Phys. Rev. B* **41** (1990) 7892.
- 25 H. J. Monkhorst and J. D. Pack: *Phys. Rev. B* **13** (1976) 5188.
- 26 K. S. Novoselov, A. K. Geim, S. V. Morozov, D. Jiang, M. I. Katsnelson, I. V. Grigorieva, S. V. Dubonos, and A. A. Firsov: *Nature* **438** (2005) 197.
- 27 C. Kittel: *Introduction to Solid State Physics* (Wiley, New York, 2005) 8th ed., p. 200.
- 28 K. Nakamura, Y. Isono, and T. Toriyama: *Jpn. J. Appl. Phys.* **47** (2008) 5132.
- 29 K. Nakamura, Y. Isono, T. Toriyama, and S. Sugiyama: *Phys. Rev. B* **80** (2009) 045205.
- 30 Z. Ni, Y. Wang, T. Yu, and Z. Shen: *Nano Res.* **1** (2008) 273.
- 31 M. A. Pimenta, G. Dresselhaus, M. S. Dresselhaus, L. G. Cançado, A. Jorio, and R. Saito: *Phys. Chem. Chem. Phys.* **9** (2007) 1276.
- 32 Z. H. Ni, T. Yu, Y. H. Lu, Y. Y. Wang, Y. P. Feng, and Z. X. Shen: *ACS Nano* **2** (2008) 2301.
- 33 Y. Y. Wang, Z. H. Ni, Z. X. Shen, H. M. Wang, and Y. H. Wu: *Appl. Phys. Lett.* **92** (2008) 043121.
- 34 A. Ismach, C. Druzgalski, S. Penwell, A. Schwartzberg, M. Zheng, A. Javey, J. Bokor, and Y. Zhan: *Nano Lett.* **10** (2010) 1542.
- 35 C. H. Lui, L. Liu, K. F. Mak, G. W. Flynn, and T. F. Heinz: *Nature* **462** (2009) 339.
- 36 E. J. Wilson: *Strain-Gauge Instrumentation: Harris' Shock and Vibration Handbook*, eds. C. M. Harris and A. G. Piersol (McGraw-Hill, New York, 2002) 5th ed., Chap. 17.
- 37 A. Fasolino, J. H. Los, and M. I. Katsnelson: *Nat. Mater.* **6** (2007) 858.

About the Authors



Mohammed Gamil received his B.S. and M.S. degrees from Benha University, Egypt, in 2005 and 2010, respectively, and his Ph.D. degree from Egypt-Japan University of Science and Technology, Egypt, in 2014 in materials science and engineering. Since 2014, he has been a lecturer at Benha University. His research interests are in MEMS, sensors, and nanotechnology. (mohammed.gamil@feng.bu.edu.eg)



Ahmed M. R. Fath El-Bab received his M.S. and Ph.D. degrees from Assiut University, Egypt, in 2002 and 2008, respectively. From 2009 to 2014, he was a lecturer (assistant professor) at Assiut University. Since 2014, he has been an associate professor at Assiut University, and currently he is also an associate professor at Egypt-Japan University of Science and Technology, Egypt. His current interests include microsensors (principle, simulation, design, and fabrication), micromachining and its application in MEMS, tactile sensing systems (tactile sensing and display), micro-energy harvesting devices, and microfluidic systems. (ahmed_rashad@yahoo.com)



Ahmed Abd El-Moneim received his B.S. and M.S. degrees from Cairo University, Egypt, in 1989 and 1993, respectively, and his Ph.D. degree from Tohoku University, Japan, in 1998. From 2010 to 2012, he was an associate professor at Egypt-Japan University of Science and Technology (E-JUST), Egypt. Since 2012, he has been a professor at E-JUST. His research is currently focused on i) the corrosion and corrosion protection of metallic structures; ii) the synthesis, characterization, and application of nanomaterials based on graphene and CNTs for liquid and hydrogen fuel production, ultra-supercapacitors, batteries, capacitive deionization, and QDSSCs; and iii) the fabrication of thermoelectric strain gauges and gas sensors. (ahmed.abdelmoneim@ejust.edu.eg)



Koichi Nakamura received his B.S., M.S., and Ph.D. degrees from Kyoto University, Japan, in 1994, 1996, and 2000, respectively, in molecular engineering. From 1999 to 2004, he was an assistant professor and, from 2004 to 2006, a senior lecturer at Kyoto University. From 2009 to 2011, he was a chair professor at Ritsumeikan University, Japan. Since 2011, he has been an associate professor at Kyoto University and an adjunct professor at Egypt-Japan University of Science and Technology, Egypt. His research interests are in quantum physics and chemistry in materials science and engineering. (koichi@cpier.kyoto-u.ac.jp)